Applied Materials Today 11 (2018) 1–6

Contents lists available at ScienceDirect

Applied Materials Today

journal homepage: www.elsevier.com/locate/apmt

Additive manufacturing of an iron-based bulk metallic glass larger than the critical casting thickness

Zaynab Mahbooba[a,b], Lena Thorsson[b], Mattias Unosson[b], Peter Skoglund[b], Harvey West[a], Timothy Horn[a], Christopher Rock[a], Evelina Vogli[c], Ola Harrysson[a,b,*]

[a] Center for Additive Manufacturing and Logistics, North Carolina State University, 126 Daniels Hall, Raleigh, NC 27607, USA
[b] Sindre Metals, 8919 Scotch Castle Drive, Raleigh, NC 27612, USA
[c] Liquidmetal Coatings, 26497 Rancho Parkway South, Lake Forest, CA 92630, USA

ARTICLE INFO

Article history:
Received 21 September 2017
Received in revised form 26 February 2018
Accepted 27 February 2018

Keywords:
Additive manufacturing
Amorphous metal
Bulk metallic glass
Fe
Direct metal laser sintering

ABSTRACT

Fe-based bulk metallic glasses (BMG) are of increasing research interest, driven in part by a unique combination of mechanical, magnetic and chemical properties. However, the maximum thickness and geometry of BMGs achievable in traditional manufacturing processes is limited. This work examines the capabilities of laser based powder bed additive manufacturing (AM) to produce relatively large Fe-based bulk metallic glass specimens. AM fabricated specimens exceed the critical casting thickness of the material by a factor of 15 or more in all dimensions. Resulting microstructural and mechanical properties are reported. Despite decreasing quench effect with increasing build thickness, X-ray diffraction analysis suggests that a fully amorphous structure was maintained throughout the build. However, a low concentration of sparsely distributed nano-grain clusters was discovered using a high-resolution electron backscatter diffraction scan. The results pave the way for novel applications of metallic glasses achievable through appropriate material design and optimization of existing additive manufacturing processes.

1. Introduction

Metallic glasses form when molten metal is rapidly solidified to avoid crystallization. Vitrification occurs when the liquid cools below the glass transition temperature with a sufficiently high rate of solidification (typically on the order of 10^5–10^8 K/s) [1–3]. Unlike crystalline metals, the atoms in metallic glasses have no long-range atomic order, however short and medium-range order has been observed [3,4].

Metallic glasses containing a ferrous transition metal (Fe, Co, or Ni) as the main constituent are highly valued for their soft magnetic properties, mechanical properties, low damping coefficient and low material cost [2]. The homogeneous glassy microstructure, free of crystalline defects, removes magnetocrystalline anisotropy resulting in low hysteresis losses [2,5,6], and the absence of grain boundaries also leads to excellent corrosion and wear resistance [1–3,5]. This unique combination of magnetic properties and high strength make Fe-based metallic glasses an optimal choice for applications such as magnetic shielding or transformer core laminations [6]. However, the requirement for rapid solidification restricts metallic glass production to relatively thin geometries using techniques such as melt spinning, vapor deposition and atomization [1,7]. These processing challenges coupled with low ductility have severely limited the potential uses of Fe-based metallic glasses as a structural material [8].

Research efforts have therefore focused on designing metallic glass alloys with greater glass forming ability (GFA). Bulk metallic glasses (BMGs) have been reported with critical cooling rates on the order of 1–10^3 K/s, and thicknesses greater than 1 cm [5,7,9]. For example, $Zr_{41}Ti_{14}Cu_{12.5}Ni_{10}Be_{22.5}$ has a maximum casting thickness between 5 and 10 cm [10]. Likewise, alloy $Fe_{48}Cr_{15}Mo_{14}C_{15}B_6Er_2$ has full amorphicity when cast in thicknesses of up to 12 mm [11]. Solidification rates necessary to obtain an amorphous microstructure impose a dimensional constraint on BMGs called the critical casting radius (R_c) [9,12]. BMGs cast into thicknesses up to the R_c will fully vitrify only if material contamination is minimized in the base material and during processing. Along with casting, powder metallurgy techniques such as hot pressing and spark plasma sintering are also used to produce BMGs. Certain strong glass forming BMGs can be produced into more complex shapes using thermoplastic forming. However, these often contain toxic (e.g. Be) or expensive elements (Pt, Pd, Au), limiting the viability of large-scale production [13].

* Corresponding author at: Center for Additive Manufacturing and Logistics, North Carolina State University, 126 Daniels Hall, Raleigh, NC 27607, USA.
E-mail address: harrysson@ncsu.edu (O. Harrysson).

https://doi.org/10.1016/j.apmt.2018.02.011
2352-9407/

Recently, researchers have attempted to produce BMGs using additive manufacturing (AM) [14–21]. A Swedish company, Exmet, was the first group to demonstrate the feasibility of this technique [22,23]. In powder bed AM, layers of metal powder ranging from approximately 20–100 μm in thickness are spread across a platform and selectively melted by a laser or electron beam energy source. The cooling rate per layer can reach 10^3–10^4 K/s, and is dependent on build parameters, layer thickness, alloy composition and part geometry. Heating and cooling rate of BMGs during AM laser processing has been modeled by [18,24–27]. The layer-by-layer melt process enables the opportunity to produce BMGs thicker than R_c, since local cooling rate is higher than the critical cooling rate. In addition, AM is able to produce near net shape components with complex and intricate geometries, unmatched by current BMG production techniques.

Jung et al. used selective laser melting (SLM) to fabricate fully amorphous FeCSiBPCrMoAl samples measuring $6 \times 2\emptyset$ mm (R_c = 3 mm) with a density of 99.7%. Despite the high density, the presence of micro-pores and fine cracking poorly affected the magnetic properties of the specimens. Cracking was attributed to thermal stresses caused by the temperature gradient between processed layer and the cold layers beneath it, and the friability of Fe-based BMGs. The authors postulated that build plate heating could potentially reduce the temperature difference between the solidified material and the melting layer to mitigate cracking [14]. Ye and Shin were able to produce crack-free FeCrMoWMnCSiB using laser direct deposition by pre-heating the build substrate to 422 °C. However, the samples were not fully amorphous due to the precipitation of a CrFe crystalline phase [17].

Most BMGs processed using powder bed AM reported in the literature did not exhibit full vitrification. For example, Zheng et al. reported crystallization in the first layer of Fe-based BMG during directed energy deposition (laser-engineered net-shaping). The fraction of the crystalline phase increased as a function of build thickness [16]. Ye and Shin observed grain nucleation exclusively in layer overlap regions where material re-melting led to devitrification [17]. Li et al. produced a heavily crystallized AlNiYCoLa BMG alloy using SLM; they showed that devitrification had resulted from chemical inhomogeneity in the melt pool caused by laser induced liquid oscillation [21]. In addition, material contamination [20] and incomplete melting of crystalline starting powder [15] have also been reported to contribute to crystallization of metallic glasses in AM.

While significant work has been contributed to the literature, no report has been identified demonstrating a fully dense and amorphous BMG produced with AM, nor have any samples exceeded the critical casting thickness, using any manufacturing method. FeCrMoCB is a well-documented glass-forming alloy [28–30] that is optimized for thermal spray applications where excellent strength and hardness are required. FeCrMoCB has a critical casting thickness <2 mm when synthesized using copper mold casting [31]. This work reports the additive manufacturing of an amorphous alloy larger than the critical casting thickness using the direct metal laser sintering (DMLS) process (Electrical Optical Systems, Krailling, Germany).

2. Materials and methods

Gas atomized FeCrMoCB powder was produced by LiquidMetal® Coatings with a nominal particle size distribution of 20–80 μm. Powder size distribution was measured using a Microtrac S3500 laser diffraction particle size analyzer, and morphology was examined using scanning electron microscopy (JEOL 6010 LA SEM). Additionally, X-ray diffraction (XRD) (Rigaku SmartLab) was used to examine the amorphicity of the powder.

Selective laser melting was performed in an EOSINT M 280 system equipped with a 200 W Yb-fiber laser. During processing, the build chamber was flooded with argon gas to limit the oxygen content (<1000 ppm). During initial process parameter development, the sample geometry consisted of 9 mm diameter cylinders 15 mm tall. These were fabricated onto stainless steel build substrates. The build substrates consisted of $15.24 \times 1.90 \times 0.63$ cm ground 4140 steel inserts, bolted into matching pockets milled into the standard EOS build platform. This setup facilitated rapid sample removal and preparation.

The build substrate temperature and layer thickness are not adjustable parameters in the EOS M 280. Pre-set equipment parameters allowed for a build plate temperature of 80 °C and layer thickness of 20 μm. The 20 μm layer thickness is smaller than the maximum particle size of the FeCrMoCB powder (20–80 μm), this is common for DMLS processing parameters. Excessively large particles will not be spread by the recoat blade. However, particles larger than 20 μm will still be used due to solidification shrinkage of the solid and powder bed densification.

A wide range of heat inputs ($I = P/vh$, where P is laser power, v is the laser scanning speed, and h is the hatch spacing) were analyzed to determine the feasible processing window for the FeCrMoCB alloy. Heat input values that drastically over- or under-melted the material were excluded from further testing. Laser power, beam speed and hatch spacing were systematically varied from 80 to 200 W, 800 to 5000 mm/s and 0.05 to 0.15 mm, respectively, using a fractional factorial design of experiments. In addition, different scanning strategies were implemented by varying the scan vector width (stripe width), scan vector overlap (stripe overlap) and the scanning pattern (hatch style).

After AM fabrication, cylinders were inspected for dislodged particles or surface cracking. Surface roughness measurements were not collected since no effort was made to optimize the parameter set that dictates roughness, the contour parameters. Density was measured using Archimedes' method in acetone, then compared to the density of a cast and hot isostatic pressed reference sample. XRD analysis was performed on cylinder cross-sections along the build plane. Based on density and XRD analyses, laser processing parameters were altered for subsequent tests, iteratively, to produce dense samples that exhibited an amorphous structure.

Based on the results of the preliminary parameter search, two cylinders measuring $30 \times 45\emptyset$ mm were produced using the optimized process settings. A low speed saw (Buehler IsoMet), was used to section one cylinder perpendicular to the build direction into three segments. These sections were examined using Archimedes density, XRD, optical and scanning electron microscopy and electron backscatter diffraction (EBSD) analyses. For SEM analysis (FEI Quanta 3D FEG), samples were ground, polished, and then etched by swabbing with aqua regia for 15 s. SEM analysis, in backscatter and secondary electron modes, was employed to visually search for a crystalline phase on the etched sample surface. Using an Oxford EBSD detector, a large surface area was manually scanned until a diffraction pattern was detected. If a grain was identified, an orientation map 1500×1500 nm was collected with a step size of 10 nm.

Vickers microhardness indentation resulted in crack initiation and growth at the indent site. Nano-indentation uses a lower load than micro-indentation, so the occurrence of cracking was reduced. Nano-indentation measurements from the polished surface of SLM-fabricated cylinders were acquired with an Anton Paar Ultra Nano-indentation Tester with a Berkovich diamond tip. The average of 21 measurements was calculated, along with elastic modulus. Coefficient of restitution (C_R) was estimated using a stainless steel ball bearing drop test on the AM bulk cylinder and compared to the same for a stainless steel surface. This approach to measuring C_R was based on previous work by Schnurmann [32].

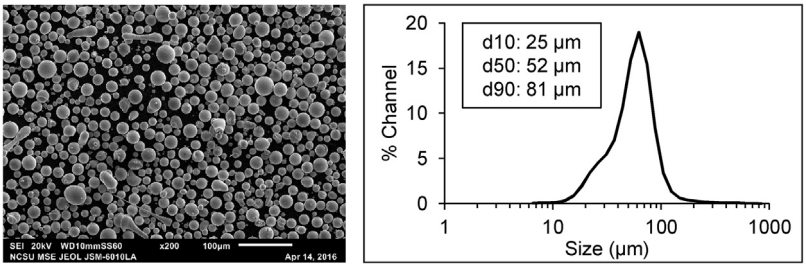

Fig. 1. Powder: Powder morphology (left) and size distribution (right) of virgin FeCrMoCB powder used for DMLS processing.

The surface of the second 45 mm diameter AM fabricated sample was polished, and an acrylic tube with an inner diameter of 45 mm and a height of 1.0 m was placed over the cylinder. A stainless steel ball bearing was dropped 0.7 m into the tube and onto the cylinder surface. The drop test was digitally recorded at 240 Hz, and frame-by-frame analysis was used to determine the drop height and bounce height. Neglecting frictional forces, C_R was calculated using, $C_R = \mathrm{sqrt}(h/H)$ where h is the first bounce height and H is the drop height. Lastly, combustion analysis was used to assess the oxygen composition of the as-fabricated bulk cylinder, as well as the feedstock powder.

3. Results

The powder size distribution of FeCrMoCB used in this study is shown in Fig. 1. The 10th and 90th percentiles are 25 µm and 81 µm, respectively. SEM analysis indicates that the powder morphology is mostly spherical, although particles exhibiting a high aspect ratio can also be observed.

During the initial laser parameter search, FeCrMoCB samples, shown in Fig. 2 (bottom), exhibited significant cracking and friability. Despite the minimal contact between the recoater blade and the FeCrMoCB sample, pieces of material were torn from cylinders during powder recoating (Fig. 2 top). Further development resulted in a processing space that consistently produced samples that matched intended geometry and build height.

Fig. 3 shows a 30 × 45Ø mm specimen. No cracking or layer delamination was evident by visual inspection of the exterior surface, but micro-cracking was observable within the bulk material during the building process. Cracking caused by a micro-indentation test, shown in Fig. 4, indicates the brittleness of the DMLS fabricated material. The XRD spectrum of the FeCrMoCB virgin powder, shown in Fig. 5, shows a wide halo peak with a low intensity corresponding to a fully amorphous structure. XRD results reported in Fig. 5 showing the bottom, middle and top sections along the 30 × 45Ø mm bulk cylinder, suggest that amorphicity was preserved during laser processing. Comparatively, a cast and hot isostatic pressed FeCrMoCB reference sample shows several sharp, high-intensity peaks corresponding to Bragg diffraction. An EBSD orientation map of a nano-grain cluster is shown in Fig. 6. Black portions represent amorphous regions of material while the colored regions are grains (d < 300 nm) that were sporadically observed in low concentrations (<1% volume) throughout the cross section of the sample.

Table 1 provides the Archimedes density measurements of the bottom, middle and top sections of the bulk cylinder as compared to a hot isostatic pressed reference. Density measurements show an increase in density with build height from 96.5% to 97.7%. Average density of the 30 × 45Ø mm cylinder is 97%. Nano-indentation testing yielded an average hardness of 9736 MPa (equivalent to HV = 902) for the DMLS-fabricated FeCrMoCB samples. In addition, nano-indentation data was used to approximate an elastic modulus of 220 GPa (Poisson's ratio was estimated at 0.3 for this alloy

Fig. 2. Process development: Photograph of DMLS samples during the early stages of process development.

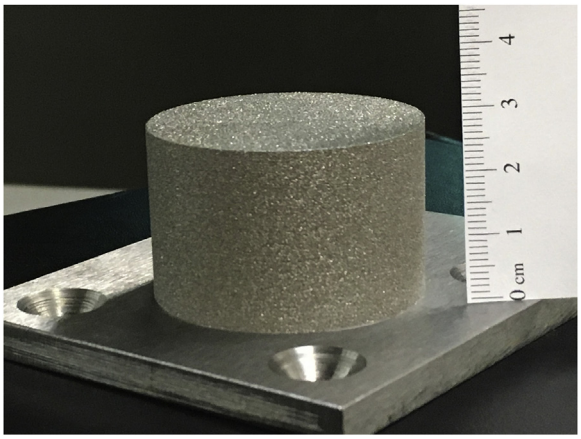

Fig. 3. DMLS-fabricated BMG: 30 × 45Ø mm FeCrMoCB bulk cylinder produced using DMLS.

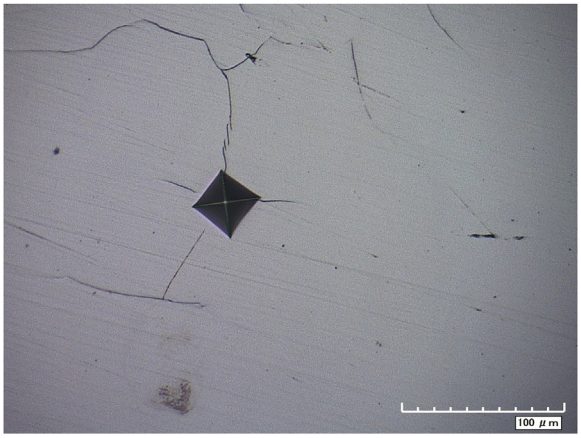

Fig. 4. Indent cracking: A micro-hardness indentation in DMLS-fabricated FeCrMoCB. Cracking caused by the indentation demonstrates the friability of FeCrMoCB.

[31]). The coefficient of restitution was estimated using a stainless steel ball bearing drop test. When dropped on the DMLS-fabricated BMG cylinder ($30 \times 45\emptyset$ mm), the ball bounced back to almost 100% of the initial drop height. Dissimilarly, the same test performed on a stainless steel surface generated a bounce only one third of the initial drop height. The coefficient of restitution for the DMLS-fabricated BMG was observed at $C_R = 0.97$, while the stainless steel test yielded $C_R = 0.60$. Furthermore, oxygen content of the virgin powder and bulk cylinder were measured at 0.087 and 0.075 at. %, respectively.

4. Discussion

Laser processing techniques, such as laser welding, laser cladding and DMLS, are associated with high residual stresses due to the large thermal gradient associated with rapid solidification. Residual stresses inherent to DMLS result in geometric distortion, layer delamination, cracking and curling. Typical post processing of DMLS-fabricated material includes a stress relieving heat treatment. It is impractical to heat treat BMGs, since heating above the crystallization temperature would induce grain nucleation and growth. The intrinsic brittleness of metallic glass amplifies the detrimental effects of residual stress build-up. For this reason, the influence of thermal stress on DMLS-fabricated FeCrMoCB was drastic. Initial processing yielded samples that were prone to severe cracking and crumbling due to high stress during processing; samples never reached intended build height or geometry. Optimized processing parameters produced parts with no obvious surface defects upon visual inspection. Researchers investigating the AM of metallic glass alloys have also experienced difficulty overcoming stress-related cracking [14,16,21].

Table 1
Archimedes density measurements of the FeCrMoCB bulk cylinder bottom, middle and top sections with standard deviation.

	Archimedes density
Top	97.7% ± 0.2%
Middle	97.1% ± 0.1%
Bottom	96.5% ± 0.0%

The alloy design of metallic glasses strongly influences the material's mechanical properties. FeC(B)-based alloys, like the material selected for this work, exhibit the highest strength and lowest ductility of the Fe-based metallic glasses [33]. An investigation on the effect of boron content on a FeC(B)-based BMGs revealed that boron additions >1.5 at.% eliminate any plastic deformation prior to failure. The fracture surface of alloys with <1.5 at. % boron exhibit a vein like pattern, indicative of plastic flow [33]. Oppositely, the FeC(B)-based alloy containing >1.5 at. % boron, like the alloy produced for this work, show no indication of plastic deformation before failure. Due to the compositionally induced brittleness of FeCrMoCB, the limited ductility inherent to BMGs and the high residual stresses in laser based processing, cracking was unavoidable during processing.

Laser heat treatment can reduce the thermal gradient between melting and solidified material, and can therefore facilitate in situ stress relief. Laser scanning pattern dictates the temperature distribution in the top layer of DMLS fabricated material. In this work, changes in laser scanning parameters diminished stresses to allow for the production of full-height, dimensionally accurate specimens. Reduction in residual stress via laser scanning pattern alteration was insufficient to eliminate the stress-induced

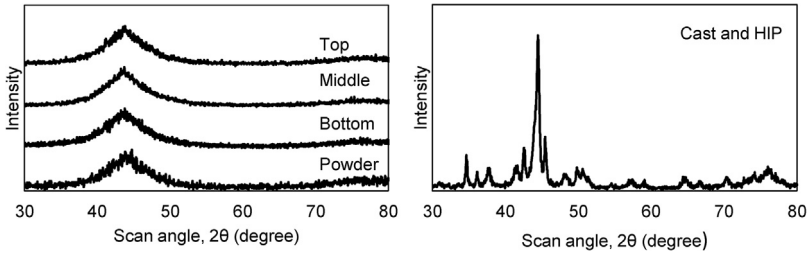

Fig. 5. X-ray diffraction: X-ray diffraction spectra of FeCrMoCB virgin powder, bulk cylinder (bottom, middle and top) and a hot isostatic pressed (HIP) reference sample.

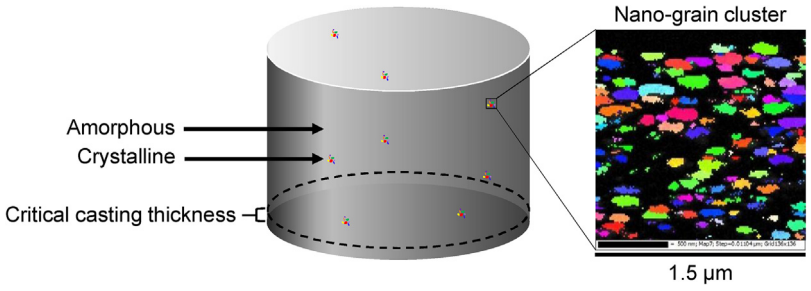

Fig. 6. Grain cluster in the bulk cylinder: EBSD micrograph collected at a nano-grain cluster in the FeCrMoCB bulk cylinder.

micro-cracking associated with rapid solidification of the low ductility FeCrMoCB alloy.

The densification of DMLS-fabricated materials is dictated by the processing parameters. Within the processing window used to produce the bulk cylinder, parameters were altered to maximize density. Increasing energy density by increasing laser power or decreasing scan speed effect the melt pool size and temperature. Too much energy input can lead to an increase in stresses or can cause beading of the molten metal as it breaks the surface tension. Too little energy input leads to incomplete melting of metal powder. Likewise, the hatch distance influences energy input into the powder bed and should be no larger than the diameter of the melt pool. The DMLS-fabricated bulk cylinder, pictured in Fig. 3, has an average density of 97%. The lack of large surface defects and high density of the cylinder suggest that the energy input was sufficient. It is likely that full density is achievable with the elimination of stress-induced micro-cracks within the bulk. Density is also influenced by the presence of spherical gas entrapment porosity, a product of gas atomization, and irregularly shaped keyhole pores. Keyhole pores are formed when the molten metal inadequately flows to fill gaps. The rapid solidification in DMLS and high viscosity of glass-forming metals do not allow adequate time for the molten material to flow into all gaps. Porosity in the DMLS cylinder was challenging to distinguish since cutting and grinding of the material induced cracking. Density measurements presented in Table 1 show an increase in density with sample height. As build height increases, poor heat transfer through the low conductivity FeCrMoCB material causes a reduction in the cooling rate. Slower cooling rates produce fewer stresses and therefore fewer density detrimental cracks are developed. In addition, the bottom layers experience prolonged thermal cycling; this could result in a lower density due to an increase in cracking as a result of structural relaxation embrittlement.

Accordingly, the $30 \times 45\emptyset$ mm bulk cylinder showed full XRD amorphicity. Cooling rate per layer was sufficient to preserve amorphicity far above the critical casting thickness despite decreasing quench rate with build height. X-ray diffraction analysis is an accepted technique for obtaining an overview of microstructure, however, the resolution is limited. EBSD has higher resolution than XRD, and therefore can be used to detect smaller grains within the microstructure. EBSD analysis revealed the presence of a low concentration of nano-grain clusters Temperature, contamination and mechanical stress are the predominant forces driving nucleation in metallic glasses [34]. Prolonged heat exposure and thermal cycling during AM are probable causes of nanocrystal nucleation. EBSD analysis showed that nano-grains exist only in localized clusters throughout the bulk FeCrMoCB cylinder; however, grain nucleation as a result of thermal annealing typically exhibits uniformly distributed grains [7]. Additionally, despite the directionality of heat flow in AM, nano-grains imaged are relatively equiaxial. Based on the localized and equiaxial nature of the nano-grains, it is unlikely that thermal annealing during DMLS processing provided the energy for grain nucleation. Alternatively, nucleation was possibly a result of oxygen contamination and/or mechanical stress.

Along with thermal annealing, impurities such as oxygen, can also induce crystallization in BMGs. Oxides act as heterogeneous nucleation sites and impact the glass formability. Furthermore, oxygen can promote the formation of metastable quasicrystalline phases that have a lower activation energy than a competing primary crystalline phase [35,36]. While it is well established that low concentrations of oxygen impurities have a detrimental effect on GFA in Zr-based metallic glasses [37,38], limited information is available on the role of oxygen in Fe-based BMGs. Li et al. report that oxygen additions between 0.02 and 0.15 at. % actually improved the GFA in a FeMoCSiBP BMG [36]. It was suggested that the critical level of oxygen depressed the liquidus temperature and suppressed precipitation of a primary phase. In any case, oxygen concentrations >0.15 at.% promoted the formation of oxygen rich crystals and reduced the GFA [36]. Similar results are reported for a FeNiPC BMG, for which oxygen additions up to 0.0252 at.% improved thermal stability and did not induce crystallization [37]. A concentration of 0.075 at.% was measured in the DMLS-fabricated FeCrMoCB material. This oxygen concentration is within the range of oxygen additions that improved GFA for FeMoCSiBP. It is possible that oxygen contamination did not induce crystallization in this work; however, a comprehensive study of oxygen in FeCrMoCB would be required to assert this conclusion.

Mechanical stress is a well-known source of localized nanocrystal nucleation in and around shear bands in amorphous metals [34,39–42]. The underlying mechanism for stress-induced grain formation is not fully understood; however, it is of general consensus that the crystallization is caused by viscous flow or local heating [34,40]. Shear band formation and propagation dictates the plasticity of metallic glasses. During plastic deformation, local strain accumulates and a shear band is developed [43]. Metallic glasses can store more elastic strain energy per unit volume than crystalline metals. When the yield strength is surpassed, the stored elastic energy dissipates inside the shear bands and can cause a drastic increase in local temperature. Lewandowski and Greer reported a temperature increase >1000 K within nanoseconds inside a shear band [44]. The adiabatic heating often results in catastrophic failure and is a probable cause of local crystallization [39,43]. In contrast, others have suggested the stress-enhanced atomic diffusion at shear bands provides enough energy for nano-grain nucleation [39,41], particularly when dynamic loading or fracture do not occur [39]. Atoms that are not in the vicinity of shear bands are not supplied with enough energy to create grains. It is reasonable to assume that the stress-induced cracking that occurred during DMLS-processing provided sufficient energy for the nucleation of nano-grain clusters.

The AM bulk FeCrMoCB cylinder hardness was 902 HV. Nano-indentation data was used to approximate an elastic modulus of 220 GPa, assuming a Poisson's ratio of 0.3. This value is in close proximity to cast BMG alloys having similar composition (Young's modulus of 190–220 GPa) [31]. Coefficient of restitution represents a dynamic and more global hardness than nano-indentation. The C_R for the DMLS fabricated BMG was observed at $C_R = 0.97$, while the stainless steel test yielded $C_R = 0.60$. This drop test demonstrates the high elastic energy storage capacity and low dissipation of the BMG fabricated in this work, even with the presence of micro-cracks, compared to stainless steel.

5. Conclusion

In this work, we demonstrate the use of DMLS to produce a fully XRD-amorphous FeCrMoCB BMG whose thickness is more than 15 times the critical casting thickness in all dimensions, and larger than any traditionally produced Fe-based BMG recorded. The DMLS-fabricated BMG is 97% dense and has no major external cracks. Due to the brittleness associated with BMGs and the FeCrMoCB alloy, DMLS process parameter alteration alone was insufficient to eliminate all micro-cracking. Therefore, stress-induced micro-cracks, a product of the rapid solidification in laser processing, are still present within the bulk material. Continued work focuses on eliminating micro-cracks by targeting Fe-based BMG alloys with enhanced plasticity. Furthermore, a low concentration of nano-grains was exposed within the BMG microstructure. The localized and isotropic nature of the nano-grains suggest that nucleation was not a product of thermal annealing. Instead, mechanical stress induced crystallization

during DMLS processing. By eliminating micro-cracks through improved alloy design, stress-induced nucleation should subside. This work proves that DMLS is a suitable technique for the development of BMGs significantly larger than their critical casting thickness with mechanical properties rivaling that of their cast counterparts.

Acknowledgements

This material is based upon work supported by the National Science Foundation under Grant no. 1,549,770 awarded to Sindre Metals, Inc., a North Carolina SME. This work was performed in part at the Analytical Instrumentation Facility (AIF) at North Carolina State University, which is supported by the State of North Carolina and the National Science Foundation (award number ECCS-1542015). The AIF is a member of the North Carolina Research Triangle Nanotechnology Network (RTNN), a site in the National Nanotechnology Coordinated Infrastructure (NNCI).

References

[1] A.L. Greer, Metallic glasses, Science 267 (1995) 1947.
[2] M. Telford, The case for bulk metallic glass, Mater. Today. 7 (2004) 36–43, http://dx.doi.org/10.1016/S1369-7021(04)00124-5.
[3] T.R. Anantharaman, Metallic Glasses: Production, Properties and Applications, Trans Tech Publications, Aedermannsdorf, Switzerland, 1984.
[4] A.L. Greer, Metallic glasses. . .on the threshold, Mater. Today. 12 (2009) 14–22, http://dx.doi.org/10.1016/S1369-7021(09)70037-9.
[5] M.F. Ashby, A.L. Greer, Metallic glasses as structural materials, Scr. Mater. 54 (2006) 321–326, http://dx.doi.org/10.1016/j.scriptamat.2005.09.051.
[6] H.H. Liebermann, I. NetLibrary, Rapidly Solidified Alloys: Processes, Structures, Properties, applications, M. Dekker, New York, 1993.
[7] A. Inoue, Stabilization of metallic supercooled liquid and bulk amorphous alloys, Acta Mater 48 (2000) 279–306, http://dx.doi.org/10.1016/S1359-6454(99)00300-6.
[8] V. Ponnambalam, S.J. Poon, G.J. Shiflet, Fe-based bulk metallic glasses with diameter thickness larger than one centimeter, J. Mater. Res. 19 (2004) 1320–1323, http://dx.doi.org/10.1557/JMR.2004.0176.
[9] W.H. Wang, C. Dong, C.H. Shek, Bulk metallic glasses, Mater. Sci. Eng. R Rep. 44 (2004) 45–89, http://dx.doi.org/10.1016/j.mser.2004.03.001.
[10] A. Peker, W.L. Johnson, A highly processable metallic glass: Zr41.2Ti13.8Cu12.5Ni10.0Be22.5, Appl. Phys. Lett. 63 (1993) 2342–2344, http://dx.doi.org/10.1063/1.110520.
[11] X.J. Gu, S.J. Poon, G.J. Shiflet, Mechanical properties of iron-based bulk metallic glasses, J. Mater. Res. 22 (2007) 344–351, http://dx.doi.org/10.1557/jmr.2007.0036.
[12] W.L. Johnson, Bulk amorphous metal – an emerging engineering material, JOM 54 (2002) 40–43, http://dx.doi.org/10.1007/BF02822619.
[13] A. Inoue, A. Takeuchi, Recent development and application products of bulk glassy alloys, Acta Mater. 59 (2011) 2243–2267, http://dx.doi.org/10.1016/j.actamat.2010.11.027.
[14] H.Y. Jung, S.J. Choi, K.G. Prashanth, M. Stoica, S. Scudino, S. Yi, U. Kühn, D.H. Kim, K.B. Kim, J. Eckert, Fabrication of Fe-based bulk metallic glass by selective laser melting: a parameter study, Mater. Des. 86 (2015) 703–708, http://dx.doi.org/10.1016/j.matdes.2015.07.145.
[15] V.K. Balla, A. Bandyopadhyay, Laser processing of Fe-based bulk amorphous alloy, Surf. Coat. Technol. 205 (2010) 2661–2667, http://dx.doi.org/10.1016/j.surfcoat.2010.10.029.
[16] B. Zheng, Y. Zhou, J.E. Smugeresky, E.J. Lavernia, Processing and behavior of Fe-based metallic glass components via laser-engineered net shaping, Metall. Mater. Trans. A. 40 (2009) 1235–1245, http://dx.doi.org/10.1007/s11661-009-9828-y.
[17] X. Ye, Y.C. Shin, Synthesis and characterization of Fe-based amorphous composite by laser direct deposition, Surf. Coat. Technol. 239 (2014) 34–40, http://dx.doi.org/10.1016/j.surfcoat.2013.11.013.
[18] G. Yang, X. Lin, F. Liu, Q. Hu, L. Ma, J. Li, W. Huang, Laser solid forming Zr-based bulk metallic glass, Intermetallics 22 (2012) 110–115, http://dx.doi.org/10.1016/j.intermet.2011.10.008.
[19] H. Sun, K.M. Flores, Microstructural analysis of a laser-processed Zr-based bulk metallic glass, Metall. Mater. Trans. A 41 (2010) 1752–1757, http://dx.doi.org/10.1007/s11661-009-0151-4.
[20] S. Pauly, L. Löber, R. Petters, M. Stoica, S. Scudino, U. Kühn, J. Eckert, Processing metallic glasses by selective laser melting, Mater. Today. 16 (2013) 37–41, http://dx.doi.org/10.1016/j.mattod.2013.01.018.
[21] X.P. Li, C.W. Kang, H. Huang, L.C. Zhang, T.B. Sercombe, Selective laser melting of an Al86Ni6Y4.5Co2La1.5 metallic glass: processing, microstructure evolution and mechanical properties, Mater. Sci. Eng. A 606 (2014) 370–379, http://dx.doi.org/10.1016/j.msea.2014.03.097.
[22] A. Langlet, Method of producing products of amorphous metal, US8052923 B2, 2011. http://www.google.com/patents/US8052923 (accessed 25.01.18).
[23] P. Skoglund, A. Langlet, Method of producing objects containing nano metal or composite metal, US8333922 B2, 2012. http://www.google.com/patents/US8333922.
[24] Y. Zhang, X. Lin, L. Wang, L. Wei, F. Liu, W. Huang, Microstructural analysis of Zr55Cu30Al10Ni5 bulk metallic glasses by laser surface remelting and laser solid forming, Intermetallics 66 (2015) 22–30, http://dx.doi.org/10.1016/j.intermet.2015.06.007.
[25] S. Guo, M. Wang, Z. Zhao, Y.Y. Zhang, X. Lin, W.D. Huang, Molecular dynamics simulation on the micro-structural evolution in heat-affected zone during the preparation of bulk metallic glasses with selective laser melting, J. Alloys Compd. (2016), http://dx.doi.org/10.1016/j.jallcom.2016.11.393.
[26] Y. Lu, H. Zhang, H. Li, H. Xu, G. Huang, Z. Qin, X. Lu, Crystallization prediction on laser three-dimensional printing of Zr-based bulk metallic glass, J. Non-Cryst. Solids. 461 (2017) 12–17, http://dx.doi.org/10.1016/j.jnoncrysol.2017.01.038.
[27] Y. Shen, Y. Li, H.-L. Tsai, Evolution of crystalline phase during laser processing of Zr-based metallic glass, J. Non-Cryst. Solids. (2017), http://dx.doi.org/10.1016/j.jnoncrysol.2017.11.001.
[28] S.J. Pang, T. Zhang, K. Asami, A. Inoue, Bulk glassy Fe–Cr–Mo–C–B alloys with high corrosion resistance, Corros. Sci. 44 (2002) 1847–1856, http://dx.doi.org/10.1016/S0010-938X(02)00002-1.
[29] Z. Zhou, L. Wang, D.Y. He, F.C. Wang, Y.B. Liu, Microstructure and wear resistance of Fe-based amorphous metallic coatings prepared by HVOF thermal spraying, J. Therm. Spray Technol. 19 (2010) 1287–1293, http://dx.doi.org/10.1007/s11666-010-9556-2.
[30] G.A. Croopnick, Iron-chromium-molybdenum-based thermal spray powder and method of making of the same, US20130052361 A1, 2013. http://www.google.com/patents/US20130052361 (accessed 25.01.18).
[31] C. Suryanarayana, A. Inoue, Iron-based bulk metallic glasses, Int. Mater. Rev. 58 (2013) 131–166, http://dx.doi.org/10.1179/1743280412Y.0000000007.
[32] R. Schnurmann, Rate of energy loss from rebounding steel balls, Proc. Phys. Soc. 53 (1941) 662, http://dx.doi.org/10.1088/0959-5309/53/6/305.
[33] C. Su, Y. Chen, P. Yu, M. Song, W. Chen, S.F. Guo, Linking the thermal characteristics and mechanical properties of Fe-based bulk metallic glasses, J. Alloys Compd. 663 (2016) 867–871, http://dx.doi.org/10.1016/j.jallcom.2015.12.196.
[34] J.-C. Lee, Y.-C. Kim, J.-P. Ahn, H.-S. Kim, S.-H. Lee, B.-J. Lee, Deformation-induced nanocrystallization and its influence on work hardening in a bulk amorphous matrix composite, Acta Mater. 52 (2004) 1525–1533, http://dx.doi.org/10.1016/j.actamat.2003.11.034.
[35] H. Li, Z. Lu, S. Yi, Estimation of the glass forming ability of the Fe-based bulk metallic glass Fe68.8C7.0Si3.5B5.0P9.6Cr2.1Mo2.0Al2.0 that contains non-metallic inclusions, Metals Mater. Int. 15 (2009) 7, http://dx.doi.org/10.1007/s12540-009-0007-x.
[36] H.X. Li, J.E. Gao, Z.B. Jiao, Y. Wu, Z.P. Lu, Glass-forming ability enhanced by proper additions of oxygen in a Fe-based bulk metallic glass, Appl. Phys. Lett. 95 (2009) 161905, http://dx.doi.org/10.1063/1.3248186.
[37] H.X. Li, C.Q. Li, D. Cao, W.M. Yang, Q. Li, Z.P. Lu, Influences of oxygen on plastic deformation of a Fe-based bulk metallic glass, Scr. Mater. 135 (2017) 24–28, http://dx.doi.org/10.1016/j.scriptamat.2017.03.018.
[38] C.T. Liu, M.F. Chisholm, M.K. Miller, Oxygen impurity and microalloying effect in a Zr-based bulk metallic glass alloy, Intermetallics 10 (2002) 1105–1112, http://dx.doi.org/10.1016/S0966-9795(02)00131-0.
[39] J.-J. Kim, Y. Choi, S. Suresh, A.S. Argon, Nanocrystallization during nanoindentation of a bulk amorphous metal alloy at room temperature, Science 295 (2002) 654–657, http://dx.doi.org/10.1126/science.1067453.
[40] Z. Yan, K. Song, Y. Hu, F. Dai, Z. Chu, J. Eckert, Localized crystallization in shear bands of a metallic glass, Sci. Rep. 6 (2016) 19358, http://dx.doi.org/10.1038/srep19358.
[41] W.H. Jiang, M. Atzmon, Mechanical strength of nanocrystalline/amorphous Al90Fe5Gd5 composites produced by rolling, Appl. Phys. Lett. 86 (2005) 151916, http://dx.doi.org/10.1063/1.1897434.
[42] H. Chen, Y. He, G.J. Shiflet, S.J. Poon, Deformation-induced nanocrystal formation in shear bands of amorphous alloys, Nature 367 (1994) 541–543, http://dx.doi.org/10.1038/367541a0.
[43] E.S. Park, Understanding of the shear bands in amorphous metals, Appl. Microsc. 45 (2015) 63–73, http://dx.doi.org/10.9729/AM.2015.45.2.63.
[44] J.J. Lewandowski, A.L. Greer, Temperature rise at shear bands in metallic glasses, Nat. Mater. 5 (2006) 15–18, http://dx.doi.org/10.1038/nmat1536.